Check for updates

VIP **Li–S batteries** *Very Important Paper*

Delocalized Isoelectronic Heterostructured FeCoO$_x$S$_y$ Catalysts with Tunable Electron Density for Accelerated Sulfur Redox Kinetics in Li-S batteries

Peng Chen, Tianyi Wang,* Di He, Ting Shi, Manfang Chen, Kan Fang, Hongzhen Lin, Jian Wang,* Chengyin Wang, and Huan Pang*

Abstract: High interconversion energy barriers, depressive reaction kinetics of sulfur species, and sluggish Li$^+$ transport inhibit the wide development of high-energy-density lithium sulfur (Li–S) batteries. Herein, differing from random mixture of selected catalysts, the composite catalyst with outer delocalized isoelectronic heterostructure (DIHC) is proposed and optimized, enhancing the catalytic efficiency for decreasing related energy barriers. As a proof-of-content, the FeCoO$_x$S$_y$ composites with different degrees of sulfurization are fabricated by regulating atoms ratio between O and S. The relationship of catalytic efficiency and principal mechanism in DIHCs are deeply understood from electro-chemical experiments to in situ/operando spectral spectroscopies i.e., Raman, XRD and UV/Vis. Consequently, the polysulfide conversion and Li$_2$S precipitation/dissolution experiments strongly demonstrate the volcano-like catalytic efficiency of various DIHCs. Furthermore, the FeCoO$_x$S$_y$-decorated cell delivers the high performance (1413 mAh g^{-1} at 0.1 A g^{-1}). Under the low electrolyte/sulfur ratio, the high loading cell stabilizes the areal capacity of 6.67 mAh cm^{-2} at 0.2 A g^{-1}. Impressively, even resting for about 17 days for possible polysulfide shuttling, the high-mass-loading FeCoO$_x$S$_y$-decorated cell stabilizes the same capacity, showing the practical application of the DIHCs in improving catalytic efficiency and reaching high electrochemical performance.

Introduction

Heterostructures consisted of two materials at the interface have present and great functionalities in electronic and optical properties. Among them, the metal-based hetero-structures have aroused wide attentions because of electronic tunability, leading to the formation of the built-in electric field (BIEF).[1–2] Generally, according to the electronic/chemical surroundings between inner core and outer coordination, the metal-based heterostructure can be div-ided into electron-donor and electron-acceptor typed heter-ostructure catalysts, as illustrated in Figure S1. Based on the change of valence electron number, the strong separation of electron-hole pairs is promoted, and a strong BIEF is constructed, which is conducive to accelerate the reaction rate.[3–8] However, the strong BIEF requires a large current density to promote the continuous separation of electrons and holes, costing extra energy. In the batteries, these two kinds of heterostructure catalysts could only form and exhibit the single-way BIEF, that is to say, these catalysts

[*] P. Chen, Prof. T. Wang, D. He, C. Wang, Prof. H. Pang
Institute for Innovative Materials and Energy, Faculty of Chemistry and Chemical Engineering
Yangzhou University
Yangzhou 225002 (China)
E-mail: wangty@yzu.edu.cn
        panghuan@yzu.edu.cn

Prof. H. Lin, Dr. J. Wang
i-Lab and CAS Key Laboratory of Nanophotonic Materials and Devices
Suzhou Institute of Nano-tech and Nano-bionics
Chinese Academy of Sciences
Suzhou 215123 (China)
E-mail: jian.wang@kit.edu

Dr. J. Wang
Helmholtz Institute Ulm (HIU)
Ulm D-89081 (Germany)

T. Shi
State Key Laboratory of Material Processing and Die and Mould Technology
School of Materials Science and Engineering
Huazhong University of Science and Technology
Wuhan 430074 (China)

Prof. M. Chen
National Base for International Science & Technology Cooperation
School of Chemistry
Xiangtan University
Xiangtan 411105 (China)

Dr. K. Fang
School of Materials Science and Engineering
Harbin Institute of Technology (Shenzhen)
Shenzhen 518055 (China)

can not realize the bifunctional catalytic capability in both charge and discharge processes. Thus, it is beneficial and desired to develop a third high-efficient catalyst to delocalize the electronic distribution with more formed active sites (Figure 1a), generating high catalytic efficiency.[9–13]

Lithium-sulfur (Li–S) batteries are deemed as the potential energy storage systems for achieving high energy density for future vehicles. However, the sluggish transformations of lithium polysulfides (LiPSs, Li_2S_n, $4 \leq n \leq 8$) and depressive reaction kinetics involving solid–liquid-solid phase changes would make the slow reaction kinetics and severe polysulfide shuttling, significantly reducing sulfur utilization and capacity.[14–18] To decrease these conversion reaction barriers, the electrochemical catalysts are widely designed and applied from metal-based compounds to single metal atoms.[19–21] However, most of catalysts play the sole function in propelling sulfur reduction or sulfide oxidation, which is attributed to the fixed BIEF in the catalyst interior. Therefore, to fully achieve high performance in charging and discharging processes, the multi-component heterojunction catalysts with delocalized electronic tunability are requested to accelerate the kinetics of sulfur redox reactions (Figure S2).[22–29]

Different from the single-way BIEF in conventional heterostructure catalysts, a heterostructure catalyst with adjustable electronic density is proposed by introducing the similar valent electronic elements in the structure, which is named as delocalized isoelectronic heterostructure catalyst (DIHC).[30] This allows to cost less energy to construct the bidirectional BIEF, so as to achieve continuous-rapid LiPSs catalytic conversions. As a protocol, the FeCo-LDH sample is selected to imitate the DIHCs by replacing O atom with isoelectronic S atom (Iso-e S) when sulfurization. In this design, the Iso-e S ($X_s = 2.5$) prefers to displace the stable apical O ($X_o = 3.5$) sites in $FeCoO_xS_y$ DIHCs through charge transfer, inducing electron redistribution and constructing delocalized electrotonic density (Figure 1b). On the premise

of interconnecting conductive carbon nanotube (CNT) network, the high-speed electronic exchange and fast catalytic ability in Li^+ transfer are granted at the triphasic interface (Figure 1c).[31–32] With a comprehensive optimization, a volcano-like catalytic ability of serial $FeCoO_xS_y$/NC DIHCs in Li_2S_n adsorption and Li_2S potentiostatic precipitation/ dissolution is initially obtained. As a consequence, the cell based on the $FeCoO_{1.5}S_{1.0}$/NC-PP can achieve a high initial specific capacity of 1413 mAh g^{-1} at 0.1 A g^{-1}.[33–35] Furthermore, even resting over 410 h at the charging voltage of 2.3 V, a high-capacity retention rate of 81.4% is still maintained at 0.2 A g^{-1} after 100 cycles. Impressively, the high mass loading cathode with lean electrolyte stabilizes the areal capacity of 5.43 mAh cm^{-2} after 100 cycles, strongly exhibiting the superiority of $FeCoO_xS_y$/NC DIHCs in catalyzing sulfur redox as probed by in situ Raman,[36] in situ XRD[37–38] and in situ UV/Vis[39] results. Our findings broaden the concept of short-range isoelectronic heterojunction for achieving practical high-performance batteries.

Results and Discussion

The schematic synthesis illustration of the $FeCoO_xS_y$ DIHCs is depicted in Figure 2a. As a demo, initially, both Fe and Co ions are adsorbed on the acid-treated carbon nanotube via electrostatic interactions, generating the layer-structured FeCo-LDH via coprecipitation method.[40] Subsequently, mixing with sulfurization precursor of CH_4N_2S, the FeCo-LDH is partially transformed into $FeCoO_xS_y$/NC DIHC in the oven under N_2 atmosphere. By regulating the ratio between CH_4N_2S and FeCo-LDH, the isoelectronic atomic O/S ratio in the DIHCs is adjusted (see details in the Supporting Information), building the bidirectional electronic fields for sulfur redox reactions. For simplification, these optimized samples with the gradual conversion from $FeCoO_{2.5}$ to $FeCoS_2$ are identified as $FeCoO_{2.5}$/NC, Fe-
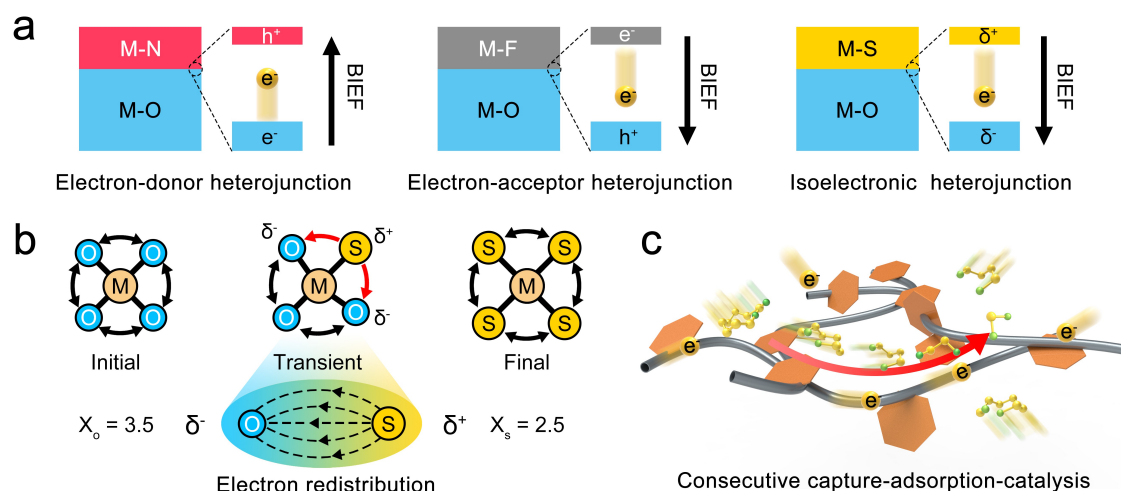

Figure 1. (a) The schematic illustration of heterostructures with different interfacial BIEF. (b) The electronic density redistribution with the introduction of isoelectronic S into the systems, inducing electron redistribution. (c) The realization of consecutive capture-adsorption-catalysis for LiPSs.
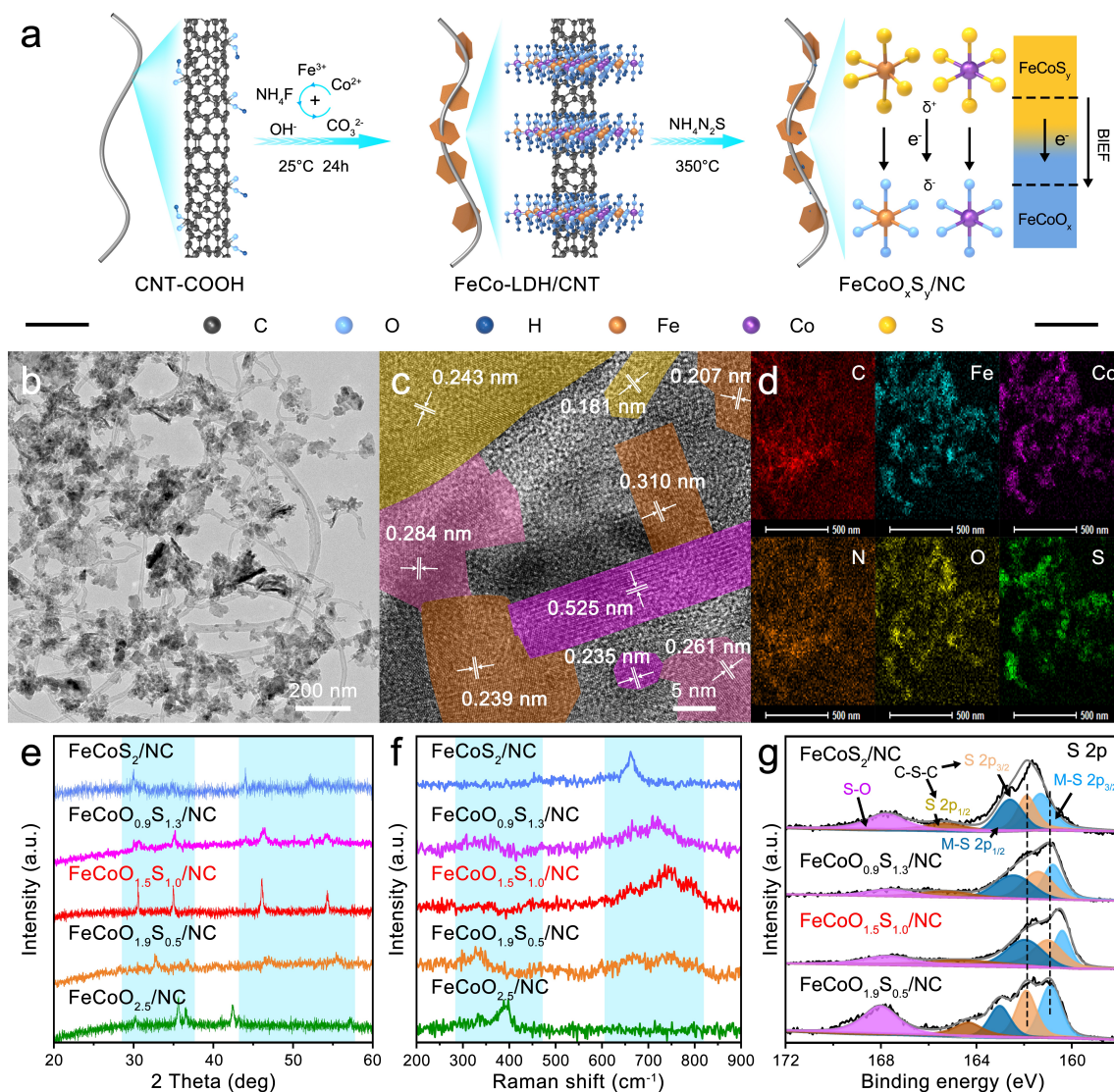
Figure 2. (a) The Illustration of synthesis process of FeCoO$_x$S$_y$/NC DIHCs. The images of (b) TEM, (c) HRTEM, and (d) elemental mappings of FeCoO$_{1.5}$S$_{1.0}$/NC DIHC, respectively. The comparisons of (e) XRD, (f) Raman, (g) S 2p XPS of various FeCoO$_x$S$_y$/NC DIHCs.

CoO$_{1.9}$S$_{0.5}$/NC, FeCoO$_{1.5}$S$_{1.0}$/NC, FeCoO$_{0.9}$S$_{1.3}$/NC and Fe-CoS$_2$/NC DIHC according to the X-ray photoelectronic spectroscopy (XPS, Details will be discussed below, Figure S3), generating different strength of the BIEF and accelerating the redox of sulfur species.

As observed in the scanning electron microscopy (SEM) and transmission electron microscopy (TEM), the morphological evolutions become significantly obvious and gradually transform from nanosheet to nanoparticle (FeCoS$_2$) when fully sulfurized (Figure S4–S5). As displayed in Figure 2b, the serial architecture is constructed by bridging nanosheet and nanoparticles with CNT in the FeCoO$_{1.5}$S$_{1.0}$/NC DIHC (Figure 2b and S6). Subsequently, in the high-resolution TEM, the overlapped coupled lattice spacing pairs are clearly verified with the apparent crystal boundary, as circled in the Figure 2c. With the help of the energy dispersive X-ray spectroscopy (EDS), the elements of Fe,

Co, O and S in the selected DIHC are well-distributed (Figure 2d and S7), indicating the successful partial sulfurization of the FeCo-LDH precursor. In comparison with the original FeCoO$_x$ one (Figure S8), many new diffraction peaks come out after partial sulfurization. Moreover, Figure 2e and S9 display that the characteristic peaks gradually shift to the left from FeCoO$_{1.9}$S$_{0.5}$/NC to FeCoS$_2$/NC, indicating that the larger Iso-e S (184 pm) replaces smaller oxygen atom (140 pm). As illustrated in Figure S10, in comparison with FeCoO$_{2.5}$ and FeCoS$_2$, the gradual substitution of Iso-e S breaks down the original balance of electronic density at the heterojunction interface and reorganizes the local charge redistribution, enhancing more catalytic sites and higher activity.[41] Further, the shifts of characteristic peaks in the Raman corresponds to the vibration changes of interatomic coupling vibration, indicating a corresponding change in atomic spacing (Figure 2f and

S11–12). Obviously, the changes in intermolecular spacing come from the difference between the ionic radius between O^{2-} and S^{2-}. The chemical surroundings of the various DIHC composites were evaluated in Figure 2g, and the corresponding fitting peaks of S $2p_{1/2}$ and $2p_{3/2}$ also shifted first towards the direction of low binding energy region and then back to the high energy region. Similarly, the binding energy variation attributed to the variation of coordination environments is also found in the XPS of Co 2p and Fe 2p (Figure S13a–b). These results indicate that the chemical interactions between Fe/Co and O/S change from the initial tensile force to the stress force as more sulfur atom in the systems. Besides, the intensity of M–O peak is weakened as gradually replaced by S (Figure S13c). Among them, the $FeCoO_{1.5}S_{1.0}$ DIHC intermediator has the largest number of isoelectronic heterojunctions and the best catalytic efficiency than others.

To further understand the delocalized electronic density distribution on regulating more catalytic sites in DIHCs, the symmetric and asymmetric cells were assembled. Initially, the polysulfide interaction experiment is carried out to see the effect of $FeCoO_xS_y/NC$ DIHCs on LiPSs (Figure 3a). After sufficiently immersing for 12 h, the solutions based on DIHCs become colorless while the $FeCoO_{1.5}S_{1.0}/NC$ one firstly reaches colorless. Meanwhile, the ultraviolet-visible (UV/Vis) results in Figure S14 also prove that the $FeCoO_xS_y/NC$ DIHC have better adsorption capability toward LiPSs. In addition, Figure 3b shows that the intensity and area of S–O peak significantly are enlarged and a distinct polythionate peak appears at 168.1 eV, demonstrating the

strong chemical interaction between LiPSs and $FeCoO_{1.5}S_{1.0}/NC$ DIHC. At the same time, the $2p_{3/2}$ peaks of both Fe and Co are shifted towards low binding energy, indicating strong interaction between bimetallic sites and negatively charged LiPSs (Figure S15).

For the cell fabrication, the DIHC was coated on the commercial PP separator and the modified $FeCoO_{1.5}S_{1.0}/NC$-PP separator still reserves excellent toughness and flexibility without any obvious crack (Figure S16–S17).[42–45] In comparison with pristine PP, the thickness of the DIHC modification layer is about 10–15 μm (Figure 3c–d). Besides, the optimal $FeCoO_{1.5}S_{1.0}/NC$-PP separator exhibits the higher affinity to the ether electrolyte with the smaller contact angle (6.9° vs. 31.9°), which helps to increase the Li^+ migration rate (Figure S18). Then, the functions of DIHC on polysulfide conversions were evaluated by symmetric cells. As shown in Figure 3e, the $FeCoO_{1.5}S_{1.0}/NC$ DIHC could accelerate the redox reaction of S_6^{2-} with obvious redox peaks and largest peak current strongly, indicating the fastest reaction kinetics and utilization of S_6^{2-}. Besides, the Li_2S precipitation kinetics was also compared on different catalytic substrates (Figure 3f and S19). As summarized in Figure 3g, the Li_2S precipitation capacity on the various DIHC shows a volcanic tendency, which is consistent with above results. For example, among them, the cell based on $FeCoO_{1.5}S_{1.0}/NC$ DIHC has the earliest nucleation response time (765 s) and highest peak current (0.37 mA), showing more polysulfides were catalytically converted into Li_2S.[46] Furthermore, the reversibility of Li_2S has the decisive role in the later capacity and lifespan. In the Li_2S dissolution
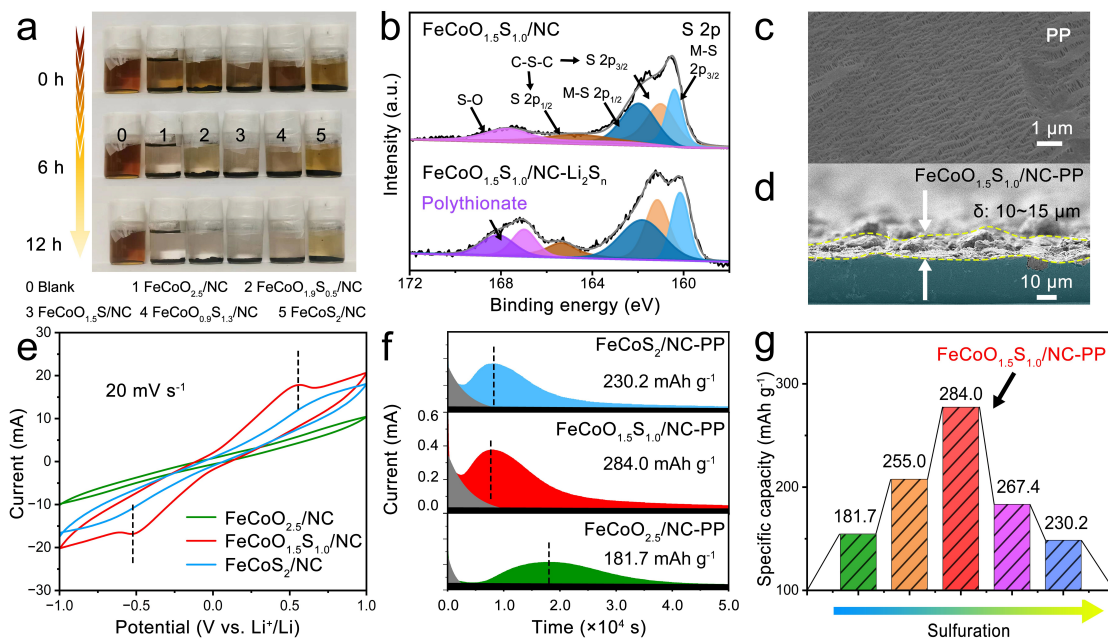

Figure 3. (a) The coloration comparison of Li_2S_n solution with the introduction of various $FeCoO_xS_y/NC$ DIHCs. (b) The corresponding S 2p XPS spectra of $FeCoO_{1.5}S_{1.0}/NC$ DIHC before and after interacting with Li_2S_n. SEM images of (c) PP and (d) $FeCoO_{1.5}S_{1.0}/NC$-PP. (e) CV curves of symmetric cells based on various catalytic electrodes. (f) Potentiostatic discharge profiles of different cells at 2.02 V and (g) the corresponding capacity summary.

experiment, the Li_2S potentiostatic charge curve and capacity is recorded and summarized (Figure S20a–f). The Li_2S conversion capacity on the various DIHC shows a volcanic tendency (313.2, 392.8, 513.5, 460.3, 356.3 mAh g^{-1}, respectively), indicating the more Li_2S is transformed to polysulfide or sulfur when charging. Meanwhile, the cell based on $FeCoO_{1.5}S_{1.0}$/NC DIHC has the earliest response time (320 s) and highest peak current (1.5 mA), showing Li_2S was catalytically converted into Li_2S_n quickly by DIHCs. Combined with XPS, Raman and catalytic investigation results, being replaced by Iso-e S, the optimal catalysts lead to the improvement of catalytic activity by redistributing electronic density around catalysts.

Later, the bidirectional catalytic ability of DIHC is also reflected in full cells with different $FeCoO_xS_y$/NC-PP separators. The electrochemical impedance spectroscopy (EIS) in Figure 4a and S21–22 shows that the $FeCoO_{1.5}S_{1.0}$/NC-one has the smallest charge transfer resistance of 20.26 Ω and the fastest Li$^+$ diffusion rate in the low-frequency region, much smaller than others, indicating the fast kinetics propelled by DIHC. Cycled at 0.1 mV s^{-1}, the cell with $FeCoO_{1.5}S_{1.0}$/NC-PP has the largest peak current and the narrowest polarization voltage gap (Figure 4b and

S23).[47–48] The rate performance tests are also used to verify the catalytic ability of $FeCoO_xS_y$/NC DIHCs to inhibit the shuttle effect of LiPSs and accelerate LiPSs reaction kinetics. As shown in Figure 4c and S24, the cell based on $FeCoO_{1.5}S_{1.0}$/NC-PP separator exhibits excellent rate capacities of 1413, 911, 713 and 524 mAh g^{-1} at 0.1, 0.5, 2.0 and 4.0 A g^{-1}. Recovering to 0.2 A g^{-1}, the specific capacity of 1028 mAh g^{-1} is restored, indicating the reversibility. Activated at 0.1 A g^{-1}, the cell based on $FeCoO_{1.5}S_{1.0}$/NC-PP separator has the initial specific capacity of 1413 mAh g^{-1} and the lowest polarization voltage (Figure 4d and S25). It is worth mentioning that below 1.9 V, the reduction of $LiNO_3$ and the electrochemical transformations between Li_2S_2 and Li_2S will take place simultaneously. However, the capacity of $LiNO_3$ decomposition contributes equally to the cells and the net increased capacity should be ascribed to the faster conversion kinetics accelerated by the $FeCoO_{1.5}S_{1.0}$/NC DIHCs. Even further cycled at 1.0 A g^{-1}, the reversible specific capacity of 525 mAh g^{-1} is achieved after 500 cycles, corresponding to capacity retention rate of 73.1 %, much higher than the controlled ones (Figure 4e and Figure S26). Indicating our DIHC catalyst is rather stable during the electrochemical lithiation/delithiation process. And then, the
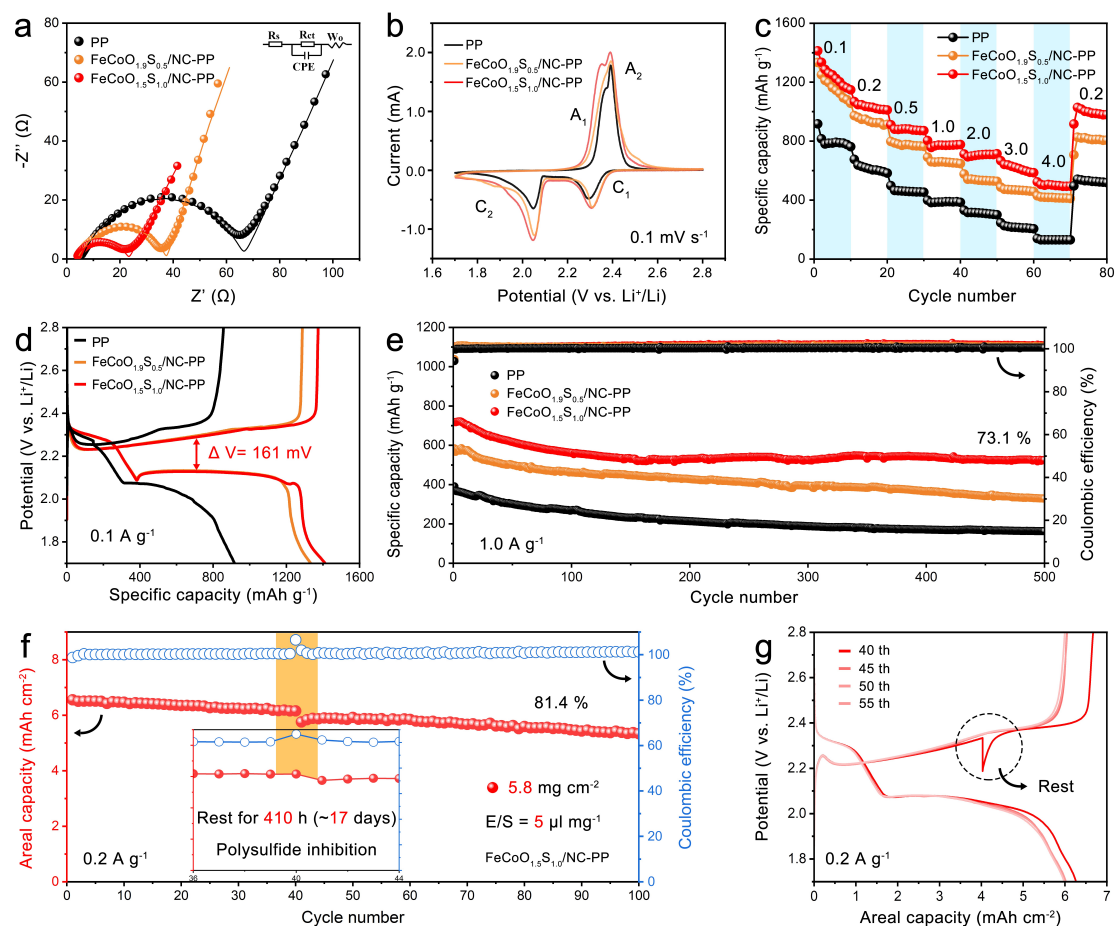

Figure 4. Comparisons of (a) EIS, (b) CV curves, (c) rate capability, and (d) galvanostatic charge/discharge profiles with/without different DIHCs. (e) Long-term cycling stability of the cells with/without DIHCs. (f) Cycling performance of Li–S battery based on $FeCoO_{1.5}S_{1.0}$/NC-PP separator with high sulfur loading (5.8 mg cm^{-2}) and low E/S (5 μL mg^{-1}). (g) The voltage profiles before and after 410 h shelving.
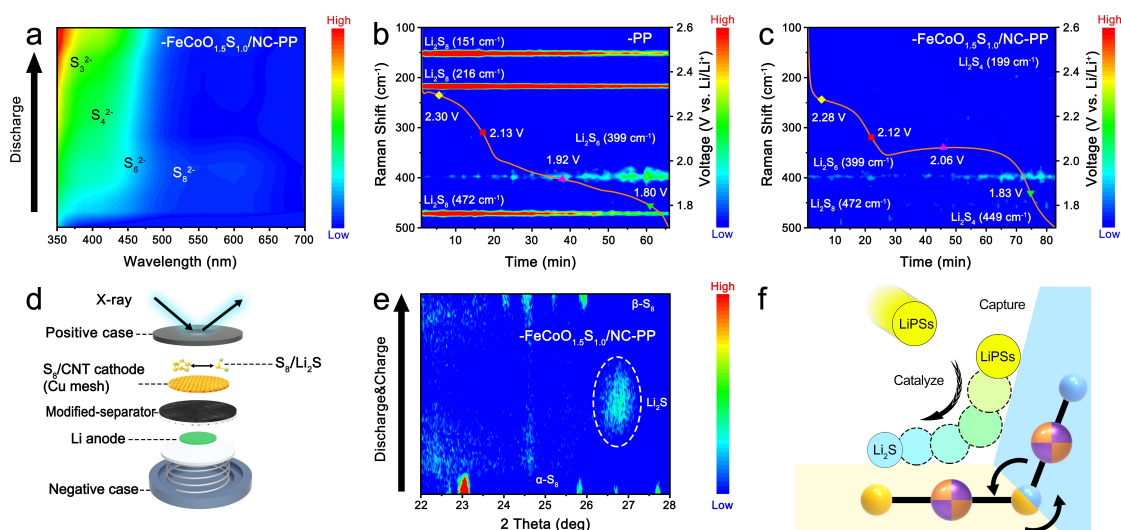
Figure 5. in situ (a) UV/Vis. (b–c) Raman. (d–e) XRD. (f) Schematic diagram of the mechanism by which the $FeCoO_{1.5}S_{1.0}$ DIHC achieve continuous capture-catalysis of LiPSs by inducing local electron redistribution.

interactions between polysulfide and DIHC are also investigated by SEM (Figure S27). In comparison with the pristine DIHC, no apparent changes are observed in the SEM image, suggesting the reserved structure.

For the practical application, the high mass loading with low electrolyte/sulfur ratio (E/S) and low self-discharge rate are obligatory. Figure 4f displays that the high-mass-loading cell ($5.8\ mg\,cm^{-2}$) based on $FeCoO_{1.5}S_{1.0}$/NC-PP separator releases a high initial capacity of $6.67\ mAh\,cm^{-2}$ at $0.2\ A\,g^{-1}$ under the low E/S ratio of 5. Moreover, the areal capacity of $5.43\ mAh\,cm^{-2}$ is still retained after 100 cycles, corresponding to the energy density of $837\ Wh\,kg^{-1}$ based on the cathode including CNT/S, Super P, and PVDF (Figure S28). However, the cells based on other $FeCoO_{2.5}$/NC-PP, $FeCoO_{1.9}S_{0.5}$/NC-PP, $FeCoO_{0.9}S_{1.3}$/NC-PP, $FeCoS_2$/NC-PP DIHC only delivery the capacity of 3.70, 3.82, 4.22, $3.47\ mAh\,cm^{-2}$ after 100 cycles, respectively (Figure S29). As acknowledged, the self-discharge comes from the polysulfide shuttling and reaction with the Li anode, deteriorating the voltage and performance. After intentionally resting for 410 h (about 17 days) to fully make the potential polysulfide shuttling, the $FeCoO_{1.5}S_{1.0}$/NC DIHC cell still maintains a low self-discharge rate of only 0.015 % per hour (Figure 4g and Figure S30). The performances of the high-sulfur-loading electrode are also compared with that of recently published heterojunction materials, and the superior overall performance is achieved (Table S1 and Figure S31). This excellent performance should be attributed to the isoelectronic heterojunction exhibits excellent catalytic properties on the premise of fast electron transport and facilitate ion transport (Figure S32).

In order to further explore the principal mechanisms of $FeCoO_{1.5}S_{1.0}$/NC DIHC and the catalytic functions on LiPSs, the various electrochemical in situ characterizations such as UV/Vis, XRD and Raman were performed. The configuration of in situ UV/Vis test is depicted in Figure S33a and Video 1.[39] Both the soluble Li_2S_n are observed in the two

systems as discharging processed. However, in the $FeCoO_{1.5}S_{1.0}$/NC system, a much lower concentrations of S_8^{2-}, S_6^{2-}, S_4^{2-}, and S_3^{2-} are achieved than the PP-based cell, exhibiting the fast kinetics of Li_2S_n conversion toward Li_2S, which is also consistent with the experimental result that $FeCoO_{1.5}S_{1.0}$/NC has better Li_2S_n adsorption capacity (Figure 5a and S33b).[36] Subsequently, in the time-resolved in situ Raman spectroscopy (Figure S34), the signals of S_n^{2-} ($151\ cm^{-1}$, $216\ cm^{-1}$, $472\ cm^{-1}$) are detected from the anodic sides during the whole discharging/charging process. While, the discharge curve of the cell based on $FeCoO_{1.5}S_{1.0}$/NC-PP separator is very stable, and the signal of LiPSs is almost disappeared at the anodic side, indicating that the $FeCoO_{1.5}S_{1.0}$/NC not only inhibits LiPSs shuttling but also promotes the catalytic conversion of LiPSs (Figure 5b–c and S35). Finally, the phasic evolutions and Li_2S formation were traced by in situ XRD on the positive side (Figure 5d).[37–38] Due to the poor catalytic performance in the PP system, the α-S_8 is partially reduced to LiPSs, and then only a small part is converted to Li_2S (26.6°) (Figure 5e and S36). While, with the introduction of $FeCoO_{1.5}S_{1.0}$/NC DIHC, the sulfur active material is almost fully converted to Li_2S with strong signal intensity when discharged and returns to sulfur after fully charged. From above combined in situ characterizations, the optimized $FeCoO_{1.5}S_{1.0}$/NC DIHC is capable of inhibiting self-discharge and accelerating the redox kinetics of sulfur (Figure 5f and S37). Moreover, under the formed BIEF in DIHC by partially replaced O with Iso-e S, it induces significant charge redistribution and builds catalytic state, further enhancing catalytic activity (Figure S38).

Conclusion

In this work, a new concept of delocalized isoelectronic heterostructure catalyst is proposed to accelerate the sulfur redox kinetics. As a proof-of-concept model, various

FeCoO$_x$S$_y$ DIHCs with different degrees of sulfurization are systematically fabricated and investigated. Among them, the volcano catalytic efficiency tendency in DIHC is obtained, demonstrating that the adsorption and catalytic activity of isoelectronic heterojunction underwent "low-high-low" changes through adsorption and catalytic experiments. Consequently, in the cell with mass loading of 5.8 mg cm^{-2}, a high areal capacity of 6.67 mAh cm^{-2} is achieved at 0.2 A g^{-1} with low E/S ratio. Meanwhile, even resting for ≈17 days, the high-loading cell stabilizes the similar capacity. By the aid of in situ UV/Vis, Raman and XRD, the detailed catalytic mechanisms are probed that delocalized isoelectronic heterostructure catalyst is capable of prohibiting polysulfide mobility by fast reaction kinetics, realizing the maximum performances. Our work has pointed out a new way to regulate the local electronic density to generate more active sites, realizing the practical Li–S battery.

Acknowledgements

Conflict of Interest

The authors declare no conflict of interest.

Data Availability Statement

The data that support the findings of this study are available from the corresponding author upon reasonable request.

Keywords: Adsorption and Catalytic · Delocalized Isoelectronic Heterostructure Catalyst · Iso-e S and O · Lithium Sulfur Battery · in-Situ Characterization

[1] X. Zhao, M. Liu, Y. Wang, Y. Xiong, P. Yang, J. Qin, X. Xiong, Y. Lei, *ACS Nano* **2022**, *16*, 19959–19979.

[2] H. Li, C. Chen, Y. Yan, T. Yan, C. Cheng, D. Sun, L. Zhang, *Adv. Mater.* **2021**, *33*, 2105067.

[3] D. Lei, W. Shang, X. Zhang, Y. Li, S. Qiao, Y. Zhong, X. Deng, X. Shi, Q. Zhang, C. Hao, X. Song, F. Zhang, *ACS Nano* **2021**, *15*, 20478–20488.

[4] R. Li, X. Zhou, H. Shen, M. Yang, C. Li, *ACS Nano* **2019**, *13*, 10049–10061.

[5] Y. Song, W. Zhao, L. Kong, L. Zhang, X. Zhu, Y. Shao, F. Ding, Q. Zhang, J. Sun, Z. Liu, *Energy Environ. Sci.* **2018**, *11*, 2620–2630.

[6] L. Zhang, J. Bi, T. Liu, X. Chu, H. Lv, D. Mu, B. Wu, F. Wu, *Energy Storage Mater.* **2023**, *54*, 410–420.

[7] M. Zhao, H. J. Peng, B. Q. Li, X. Chen, J. Xie, X. Liu, Q. Zhang, J. Q. Huang, *Angew. Chem. Int. Ed.* **2020**, *59*, 9011–9017.

[8] H. Li, P. Shi, L. Wang, T. Yan, T. Guo, X. Xia, C. Chen, J. Mao, D. Sun, L. Zhang, *Angew. Chem. Int. Ed.* **2023**, *62*, 202216286.

[9] G. Y. Zhai, D. Xu, S. N. Zhang, Z. H. Xue, H. Su, Q. Y. Yu, H. H. Wang, X. Lin, Y. X. Lin, L. H. Sun, X. H. Li, J. S. Chen, *Adv. Funct. Mater.* **2020**, *30*, 2005779.

[10] D. Q. Wang, Z. Krix, O. P. Sushkov, I. Farrer, D. A. Ritchie, A. R. Hamilton, O. Klochan, *Nano Lett.* **2023**, *23*, 1705–1710.

[11] N. Agmon, *J. Am. Chem. Soc.* **2017**, *139*, 15068–15073.

[12] H. Tian, H. Tian, S. Wang, S. Chen, F. Zhang, L. Song, H. Liu, J. Liu, G. Wang, *Nat. Commun.* **2020**, *11*, 5556.

[13] H. Tian, H. Tian, W. Yang, F. Zhang, W. Yang, Q. Zhang, Y. Wang, J. Liu, S. R. P. Silva, H. Liu, G. Wang, *Adv. Funct. Mater.* **2021**, *31*, 2101796.

[14] Y. Chen, T. Wang, H. Tian, D. Su, Q. Zhang, G. Wang, *Adv. Mater.* **2021**, *33*, 2003666.

[15] M. Li, Z. Bai, Y. Li, L. Ma, A. Dai, X. Wang, D. Luo, T. Wu, P. Liu, L. Yang, K. Amine, Z. Chen, J. Lu, *Nat. Commun.* **2019**, *10*, 1890.

[16] J. Wang, J. Zhang, S. Duan, L. Jia, Q. Xiao, H. Liu, H. Hu, S. Cheng, Z. Zhang, L. Li, W. Duan, Y. Zhang, H. Lin, *Nano Lett.* **2022**, *22*, 8008–8017.

[17] J. Wang, L. Jia, S. Duan, H. Liu, Q. Xiao, T. Li, H. Fan, K. Feng, J. Yang, Q. Wang, M. Liu, J. Zhong, W. Duan, H. Lin, Y. Zhang, *Energy Storage Mater.* **2020**, *28*, 375–382.

[18] J. Zhang, C. You, H. Lin, J. Wang, *Energy Environ. Mater.* **2022**, *5*, 731–750.

[19] X. Yang, X. Gao, Q. Sun, S. P. Jand, Y. Yu, Y. Zhao, X. Li, K. Adair, L. Y. Kuo, J. Rohrer, J. Liang, X. Lin, M. N. Banis, Y. Hu, H. Zhang, X. Li, R. Li, H. Zhang, P. Kaghazchi, T. K. Sham, X. Sun, *Adv. Mater.* **2019**, *31*, 1901220.

[20] R. Zhu, W. Zheng, R. Yan, M. Wu, H. Zhou, C. He, X. Liu, C. Cheng, S. Li, C. Zhao, *Adv. Funct. Mater.* **2022**, *32*, 2207021.

[21] S. Wang, Z. Wang, F. Chen, B. Peng, J. Xu, J. Li, Y. Lv, Q. Kang, A. Xia, L. Ma, *Nano Res.* **2023**, 1998–0124.

[22] B. Jiang, D. Tian, Y. Qiu, X. Song, Y. Zhang, X. Sun, H. Huang, C. Zhao, Z. Guo, L. Fan, N. Zhang, *Nano-Micro Lett.* **2022**, *14*, 40.

[23] W. Hua, T. Shang, H. Li, Y. Sun, Y. Guo, J. Xia, C. Geng, Z. Hu, L. Peng, Z. Han, C. Zhang, W. Lv, Y. Wan, *Nat. Catal.* **2023**, *6*, 174–184.

[24] X. Sun, Y. Qiu, B. Jiang, Z. Chen, C. Zhao, H. Zhou, L. Yang, L. Fan, Y. Zhang, N. Zhang, *Nat. Commun.* **2023**, *14*, 291.

[25] W. Zhao, S. Yuan, L. Zhang, F. Jiang, Y. Yang, G. Zou, H. Hou, P. Ge, W. Sun, X. Ji, *Energy Storage Mater.* **2022**, *45*, 1183–1200.

[26] P. Chen, T. Wang, F. Tang, G. Chen, C. Wang, *Chem. Eng. J.* **2022**, *446*, 136990.

[27] D. Zhang, Y. Luo, J. Liu, Y. Dong, C. Xiang, C. Zhao, H. Shu, J. Hou, X. Wang, M. Chen, *ACS Appl. Mater. Interfaces* **2022**, *14*, 23546–23557.

[28] J. Wang, L. Li, H. Hu, H. Hu, Q. Guan, M. Huang, L. Jia, H. Adenusi, K. V. Tian, J. Zhang, S. Passerini, H. Lin, *ACS Nano* **2022**, *16*, 17729–17760.

[29] J. Wang, L. Jia, J. Zhong, Q. Xiao, C. Wang, K. Zang, H. Liu, H. Zheng, J. Luo, J. Yang, H. Fan, W. Duan, Y. Wu, H. Lin, Y. Zhang, *Energy Storage Mater.* **2019**, *18*, 246–252.

[30] Z.-K. Wang, P. Zhao, Z.-Y. Jiang, Y.-M. Lin, J.-M. Zheng, *Phys. B* **2023**, *650*, 414535.

[31] T. Wang, D. Su, Y. Chen, K. Yan, L. Yu, L. Liu, Y. Zhong, P. H. L. Notten, C. Wang, G. Wang, *Chem. Eng. J.* **2020**, *401*, 126079.

[32] Z. Chang, H. Yang, X. Zhu, P. He, H. Zhou, *Nat. Commun.* **2022**, *13*, 1510.

[33] F. Pei, L. Lin, A. Fu, S. Mo, D. Ou, X. Fang, N. Zheng, *Joule* **2018**, *2*, 323–336.

[34] H. Yang, A. Naveed, Q. Li, C. Guo, J. Chen, J. Lei, J. Yang, Y. Nuli, J. Wang, *Energy Storage Mater.* **2018**, *15*, 299–307.

[35] P. Wang, X. Dai, P. Xu, S. Hu, X. Xiong, K. Zou, S. Guo, J. Sun, C. Zhang, Y. Liu, T. Zhou, Y. Chen, *eScience* **2023**, *3*, 100088.

[36] M. Liu, P. Chen, X. Pan, S. Pan, X. Zhang, Y. Zhou, M. Bi, J. Sun, S. Yang, A. L. Vasiliev, P. J. Kulesza, X. Ouyang, J. Xu, X. Wang, J. Zhu, Y. Fu, *Adv. Funct. Mater.* **2022**, *32*, 2205031.

[37] W. Yao, J. Xu, Y. Cao, Y. Meng, Z. Wu, L. Zhan, Y. Wang, Y. Zhang, I. Manke, N. Chen, C. Yang, R. Chen, *ACS Nano* **2022**, *16*, 10783–10797.

[38] J. Conder, R. Bouchet, S. Trabesinger, C. Marino, L. Gubler, C. Villevieille, *Nat. Energy* **2017**, *2*, 17069.

[39] Z. Ma, W. Liu, X. Jiang, Y. Liu, G. Yang, Z. Wu, Q. Zhou, M. Chen, J. Xie, L. Ni, G. Diao, *ACS Nano* **2022**, *16*, 14569–14581.

[40] H. Xu, B. Wang, C. Shan, P. Xi, W. Liu, Y. Tang, *ACS Appl. Mater. Interfaces* **2018**, *10*, 6336–6345.

[41] C. Ye, H. Cheng, L. Zheng, J. Lin, Q. Xu, Y. Qiu, Z. Pan, Y. Qiu, *Nano Lett.* **2023**, *23*, 1573–1581.

[42] T. Nie, Y. Zhu, M. Fang, L. Ma, J. Xu, Y. Cao, S. Hu, X. Zhang, D. Niu, *J. Colloid Interface Sci.* **2023**, *640*, 908–916.

[43] B. Wang, Y. Ren, Y. Zhu, S. Chen, S. Chang, X. Zhoua, P. Wanga, H. Sun, X. Menga, S. Tanga, *Adv. Sci.* **2023**, *10*, 2300860.

[44] X. Li, Q. Guan, Z. Zhuang, Y. Zhang, Y. Lin, J. Wang, C. Shen, H. Lin, Y. Wang, L. Zhan, L. Ling, *ACS Nano* **2023**, *17*, 1653–1662.

[45] K. Chen, G. Zhang, L. Xiao, P. Li, W. Li, Q. Xu, J. Xu, *Small Methods* **2021**, *5*, 2001056.

[46] L. Li, H. Tu, J. Wang, M. Wang, W. Li, X. Li, F. Ye, Q. Guan, F. Zhu, Y. Zhang, Y. Hu, C. Yan, H. Lin, M. Liu, *Adv. Funct. Mater.* **2023**, *33*, 2212499.

[47] H. Ye, Y. Li, *Energy Lab.* **2022**, *1*, 220003.

[48] J. Zhang, R. He, Q. Zhuang, X. Ma, C. You, Q. Hao, L. Li, S. Cheng, L. Lei, B. Deng, X. Li, H. Lin, J. Wang, *Adv. Sci.* **2022**, *9*, 2202244.